Multibody Syst Dyn (2021) 51:195–219
https://doi.org/10.1007/s11044-020-09764-8

# Dynamic modeling, analysis, and comparative study of a quadruped with bio-inspired robotic tails

**Yujiong Liu**[1] · **Pinhas Ben-Tzvi**[1]

Received: 21 September 2019 / Accepted: 31 October 2020 / Published online: 17 November 2020


**Abstract** Looking to nature, animals frequently utilize tails to work alongside or in place of their legs to maneuver, stabilize, and/or propel to achieve highly agile motions. Although the single-link robotic tail shows its dynamical superiority and practical effectiveness in mobile platform maneuvering, most tails observed in nature have multi-link structures. Therefore, to investigate this novel tail structure, bio-inspired and biomimetic multi-link robotic tails were proposed and implemented. However, due to the lack of a whole-body dynamic model, previous research focused on investigating the tail subsystem independently without considering the mobile platform's motions, which introduces deficiencies on both analysis and control. To bridge this theoretical gap, this paper presents a unified dynamics model that incorporates both the quadruped and the tail subsystems as a complete coupled dynamic system. Classical multibody dynamics formulation based on the principle of virtual work is utilized to derive the dynamic model. Based on the new whole-body dynamic model, three typical tail structures, including a single-link pendulum tail, a multi-link rigid tail, and a multi-link flexible tail are evaluated. The results indicate that by using a center of mass-based benchmark, the multi-link tail structure is dynamically equivalent to the single-link tail structure for bending motion. However, for rolling motions, the multi-link structure illustrates noticeable dynamical benefits compared to a single-link structure due to its higher inertia. In addition, a multi-link flexible structure shows significant oscillations and uncontrollable dynamic behaviors due to its under-actuation feature, which may limit its usage for highly dynamic applications.

**Keywords** Robotic tail · Multi-link tail · Bio-inspiration · Dynamic modeling · Dynamic analysis

✉ P. Ben-Tzvi
bentzvi@vt.edu

Y. Liu
yjliu@vt.edu

[1] Mechanical Engineering Department, Virginia Tech, Blacksburg, VA 24060, USA

## 1 Introduction

The animal kingdom has always been an important source for engineering inspiration and innovation. For instance, inspired by animal tail [10], robotic tails [1–3, 6, 9, 11–13, 16, 18, 23, 27, 36, 37] are used to maneuver or stabilize a mobile platform. However, if we take a closer look at existing research and natural counterparts, it could be easily found that these robotic tails all have a single-link structure while the animal tails usually have multi-link structures. The reasons as to why animals require multi-link tails are believed to be due to their unique benefit of being versatile and dexterous, i.e., multi-link tails satisfy both the static (support and manipulation) and the dynamic (maneuvering and stabilization) requirements simultaneously for animal locomotion. For instance, depending on the situation, squirrel monkeys [35] may use their tails to grab on branches or to balance while walking. Kangaroos [5, 21] and kangaroo rats [8] are both found to use their tails as an additional support during static locomotion while using their tails to maneuver and stabilize during dynamic locomotion. Therefore, investigating animal-like multi-link robotic tails has both engineering and biological meanings.

Several multi-link [15, 17, 26, 28, 29] and continuum (infinite links) [20, 30, 32] robotic tails have been developed. Theoretical research [24] and experimental evaluation [15, 17, 26, 28, 29] both show that coupled multi-link structures (adjacent links that are coupled mechanically) have the benefit of generating higher inertia loading and volumetric center of mass (COM) workspace. Hardware in the loop experiments and simulations [25] were also conducted to investigate the stabilization and maneuvering control of legged robot locomotion by using these tails. However, previous theoretical research is either unclear (modeling the tail subsystem and the quadruped subsystem separately [15, 17, 26, 28, 29]) or not comprehensive enough (evaluating planar tail [24] and pendulum tail [14] only). This leads to two corresponding modeling issues: (1) the coupling effect between the tail subsystem and the mobile platform is not included, and (2) the general quadruped model with spatial multi-link tails is missing.

In addition, as the first step, previous control trails [25] focused on using decoupled control methods to maneuver and stabilize the legged robotic platform. This approach essentially treats the tail subsystem and the mobile platform (base) subsystem separately and injects tail dynamical loading into the base dynamics through constraint forces, which results in significant control deficiencies since in practice the tail motion is affected by the base motion. The reason for doing so is partially due to the lack of a whole-body dynamics model.

Moreover, since the success of a robotic tail focusing on agile behaviors relies heavily on its dynamic performance, the dynamics-based tail synthesis (e.g. optimal design) is more preferable than a kinematics-based synthesis. Due to the coupled motion between the mobile platform and the tail, a whole-body dynamics is required for the dynamics design. However, considering the vast design parameters and the different tail types, the traditional multibody dynamics software (e.g., MSC Adams) is neither effective nor efficient for this type of task. As a result, most of the existing tails were designed either based on empirical methods or based solely on the tail dynamics [27]. With the help of the whole system dynamics incorporating both the mobile platform subsystem and the tail subsystem, the tail synthesis task could be solved more reasonably and effectively.

Therefore, motivated by addressing the modeling issues and control deficiency for current multi-link robotic tail research, this paper aims to develop and analyze a unified dynamic model that incorporates both the multi-link tail dynamics and the legged robot dynamics. This new model could be used as a platform to investigate different tail structures and help with dynamics-based tail synthesis.

It is worth to note that to avoid the effects of the discontinuous ground contact and focus the research on the comparative study of the tail subsystems, the model in this paper fixes the four feet of the quadruped to the ground, which makes the quadruped essentially become a parallel mechanism (like a 6 degrees of freedom flight simulator). For parallel mechanisms, instead of using the floating base model [19, 22, 31] and contact constraint equations, virtual work principle-based approaches [33, 34] are more commonly used due to their easier inverse kinematics (which allows solving the closed kinematic chain in advance). Therefore, a similar virtual work-based approach is applied in this paper as the formulation framework for the quadruped-tail dynamic model.

The major contributions of this paper could be summarized into two parts. First, a novel unified dynamic model that incorporates both a quadruped and a multi-link tail is established. Because of a similar problem setting to parallel robots, virtual work-based framework and techniques are utilized for modeling. Second, based on the unified dynamic model, comparative study of three representative tail structures, namely, a single-link pendulum tail, a decoupled rolling multi-link tail, and a coupled rolling multi-link tail, is conducted. The results provide important information for future robotic tail synthesis and controller development.

This paper is organized as follows. Section 2 formulates the modeling framework based on the virtual work principle. Section 3 calculates the required kinematic terms for the quadruped subsystem and the tail subsystem. Section 4 computes the corresponding dynamic loadings and assembles the inverse and forward dynamic models. Section 5 implements the numerical experiments and conducts the comparative study for different tail structures. Section 6 summarizes the main results of this paper and provides an outline for future work.

## 2 Formulation of the unified dynamics framework using virtual work principle

This section formulates the overall dynamic modeling framework of a general 6 degrees of freedom (DOF) quadruped with three different tails using virtual work principle. Based on the virtual work principle, for an $N$ rigid body system, the equations of motion may be expressed as in Eq. (1) where $\mathbf{F}_i$, $\mathbf{M}_i$, $\mathbf{I}_i$, $\mathbf{v}_i$, and $\boldsymbol{\omega}_i$ are the active force, active moment, inertia matrix, linear velocity, and angular velocity of body $i$, respectively. The "$\sim$" symbol above a vector indicates the skew-symmetric expansion of this vector.

$$\sum_{i=1}^{N}\left[\delta\mathbf{x}_i^T\left(\mathbf{F}_i - m\dot{\mathbf{v}}_i\right) + \delta\boldsymbol{\theta}_i^T\left(\mathbf{M}_i - \mathbf{I}_i\dot{\boldsymbol{\omega}}_i - \tilde{\boldsymbol{\omega}}_i\mathbf{I}_i\boldsymbol{\omega}_i\right)\right] = 0 \tag{1}$$

Expressing the virtual displacements $\delta\mathbf{x}_i$ and $\delta\boldsymbol{\theta}_i$ by using generalized coordinates $\mathbf{q}$ and rearranging the force terms in Eq. (1) yields Eq. (2), in which $\mathbf{J}_{i,x}$ and $\mathbf{J}_{i,\omega}$ are the Jacobian matrices defined by $\delta\mathbf{x}_i = \mathbf{J}_{i,x}\delta\mathbf{q}$ and $\delta\boldsymbol{\theta}_i = \mathbf{J}_{i,\omega}\delta\mathbf{q}$, respectively. We have

$$\sum_{i=1}^{N}\left(\mathbf{J}_{i,x}^T\mathbf{F}_i + \mathbf{J}_{i,\omega}^T\mathbf{M}_i\right) = \sum_{i=1}^{N}\left[\mathbf{J}_{i,x}^T m\dot{\mathbf{v}}_i + \mathbf{J}_{i,\omega}^T(\mathbf{I}_i\dot{\boldsymbol{\omega}}_i + \tilde{\boldsymbol{\omega}}_i\mathbf{I}_i\boldsymbol{\omega}_i)\right] \tag{2}$$

Since the left hand side of Eq. (2) contains all the non-inertia forces and the right hand side contains all the inertia forces, this equation essentially means that the system input

(the "actuation") equals the system output (the "motion"), i.e. the "actuation" generates the "motion".

Based on Eq. (2), the quadruped-tail dynamics can be formulated as in Eq. (3), where $\boldsymbol{\tau}_{qa}$ is the actuation torque for the quadruped and $\boldsymbol{\tau}_{ta}$ is the actuation torque/force for the tail. $\boldsymbol{\tau}_b$, $\boldsymbol{\tau}_{l,i}$ and $\boldsymbol{\tau}_t$ are the generalized torques (includes inertia, elastic, damping loadings, etc.) contributed by the traveling plate (or torso), the $i$th leg, and the tail, respectively. $\mathbf{J}_{qa}^T$ and $\mathbf{J}_{ta}^T$ are the corresponding Jacobian matrices for the actuation torques/forces. We have

$$\mathbf{J}_{qa}^T \boldsymbol{\tau}_{qa} + \mathbf{J}_{ta}^T \boldsymbol{\tau}_{ta} = \boldsymbol{\tau}_b + \sum_{i=1}^{4} \boldsymbol{\tau}_{l,i} + \boldsymbol{\tau}_t \tag{3}$$

It is worth to note that Eq. (3) might be over-actuated or under-actuated, depending on the tail structure. For the over-actuated cases, namely, the pendulum tail case and the roll–revolute–revolute robotic tail (R3RT) [29] case, Moore–Penrose inverse might be used to invert the actuation Jacobian.

## 3 Kinematic analyses of the quadruped and tail subsystems

This section substantiates the modeling framework by developing the subsystem kinematic models of the quadruped (Sect. 3.1) and the tails (Sect. 3.2).

### 3.1 Quadruped subsystem kinematics

To investigate the tail's dynamical effects on a mobile platform, a full mobility (6 DOF) quadruped is proposed for general modeling purposes. However, to avoid the influence of the discontinuous ground contact on the tail motion, the quadruped is assumed to be standing on the ground on its four feet at all times. This specific setting avoids the discussion on complicated hybrid dynamics during locomotion, and thus makes the dynamic model a good platform to analyze the tail behaviors closely and thoroughly. The only cost of this approach is that the quadruped now becomes a parallel mechanism, for which the forward kinematics and dynamics are usually difficult to obtain.

The kinematic configuration of the tailed quadruped is shown in Fig. 1, where the robot consists of one torso, one tail, and four identical legs. To be consistent with the traditional parallel mechanism terminology, the torso is also referred to as the traveling plate in this paper. Each leg consists of a *SRRR* kinematic chain in which the universal joint on the hip is decomposed into two intersecting revolute joints and the feet are modeled as spherical joints. $\Sigma S := (S, \mathbf{x}_s, \mathbf{y}_s, \mathbf{z}_s)$ is the inertial frame on the ground and $\Sigma P := (P, \mathbf{x}_p, \mathbf{y}_p, \mathbf{z}_p)$ is the body fixed frame of the traveling plate, with its origin at the traveling plate center $P$ and its orientation along with the traveling plate edges.

The tail subsystem is connected to the body at point $T$ and will be substantiated in Sect. 3.2 by actual tail models. Since there are 6 DOF for the quadruped, $\mathbf{q} = [\mathbf{p}^T \quad \boldsymbol{\phi}^T \quad \mathbf{q}_t^T]^T$ is chosen as the independent generalized coordinate set, where $\mathbf{p}$ is the position vector of point $P$, and $\boldsymbol{\phi} = [\phi_x \quad \phi_y \quad \phi_z]^T$ are the rotational angles of the traveling plate with respect to $\mathbf{x}_s$, $\mathbf{y}_s$, and $\mathbf{z}_s$, respectively. $\mathbf{q}_t$ represents the generalized coordinate of the tail with $m$ components, i.e. the tail subsystem has $m$ DOFs. Therefore, the rotation matrix ${}^S\mathbf{R}_P$ from frame $\Sigma P$ to $\Sigma S$ could be calculated by Eq. (4), where the notations "$c$"

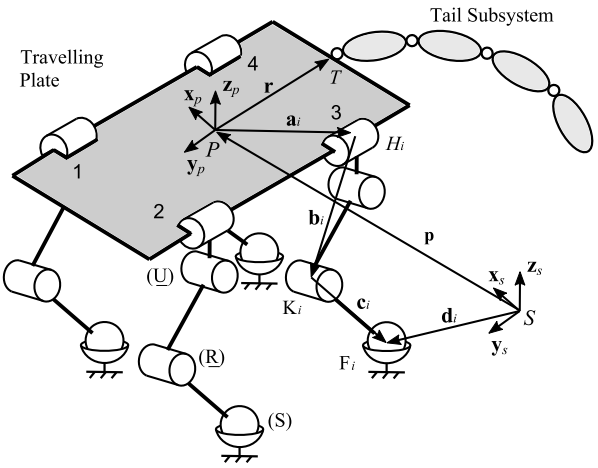


**Fig. 1** The kinematic configuration of a quadruped with a multi-link tail

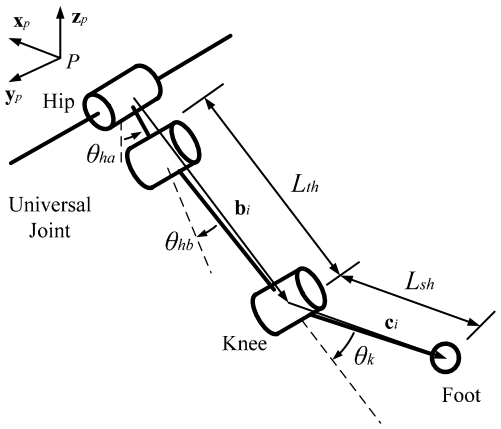


**Fig. 2** Kinematic parameters of leg *i*

and "*s*" are the abbreviated form for the cosine and sine functions, respectively.

$$ {}^{S}\mathbf{R}_P = \begin{bmatrix} c\phi_z c\phi_y & c\phi_z s\phi_y s\phi_x - s\phi_z c\phi_x & c\phi_z s\phi_y c\phi_x + s\phi_z s\phi_x \\ s\phi_z c\phi_y & s\phi_z s\phi_y s\phi_x + c\phi_z c\phi_x & s\phi_z s\phi_y c\phi_x - c\phi_z s\phi_x \\ -s\phi_y & c\phi_y s\phi_x & c\phi_y c\phi_x \end{bmatrix} \tag{4} $$

The angular velocity and angular acceleration of the traveling plate in the inertial frame $\Sigma S$ could then be obtained using Eq. (5) and Eq. (6):

$$ \boldsymbol{\omega} = \begin{bmatrix} \dot{\phi}_x & \dot{\phi}_y & \dot{\phi}_z \end{bmatrix}^T \tag{5} $$

$$ \dot{\boldsymbol{\omega}} = \begin{bmatrix} \ddot{\phi}_x & \ddot{\phi}_y & \ddot{\phi}_z \end{bmatrix}^T \tag{6} $$

### *3.1.1 Position analysis of leg i*

Since the quadruped is essentially a parallel mechanism consisting of four closed chains, the inverse kinematics need be solved first. For each leg, the joint angles are defined as in Fig. 2,

where $\theta_{ha,i}, \theta_{hb,i} \in (-\pi/2, \pi/2)$ and $\theta_{k,i} \in (-\pi/2, 0)$. Based on the kinematic configuration in Fig. 1, the vector loop constraint of leg $i$ is given by Eq. (7).

$$\mathbf{b}_i + \mathbf{c}_i = \mathbf{d}_i - \mathbf{p} - \mathbf{a}_i \tag{7}$$

Express Eq. (7) in frame $\Sigma P$ and denote $\mathbf{s}_i = {}^P\mathbf{d}_i - {}^P\mathbf{p} - {}^P\mathbf{a}_i$. Since $\mathbf{s}_i$ is a known vector and ${}^P\mathbf{b}_i$, ${}^P\mathbf{c}_i$ contain the three unknown revolute joint angles $\theta_{ha,i}$, $\theta_{hb,i}$ and $\theta_{k,i}$, Eq. (7) is fully defined and may be solved as

$$\theta_{ha,i} = \tan^{-1}\frac{s_{ix}}{s_{iz}} \tag{8}$$

$$\theta_{hb,i} = \cos^{-1}\frac{L_{th}^2 + \|\mathbf{s}_i\|^2 - L_{sh}^2}{2L_{th}\|\mathbf{s}_i\|} + \sin^{-1}\frac{s_{iy}}{\|\mathbf{s}_i\|} \tag{9}$$

$$\theta_{k,i} = \cos^{-1}\frac{L_{th}^2 + L_{sh}^2 - \|\mathbf{s}_i\|^2}{2L_{th}L_{sh}} - \pi \tag{10}$$

where $s_{ix}$, $s_{iy}$, and $s_{iz}$ are the $x$, $y$, and $z$ component of $\mathbf{s}_i$, respectively.

### *3.1.2 Joint Jacobian matrices of leg i*

Since the actuators are directly attached to the leg joints, the joint Jacobian matrices for each leg are required to map the actuator inputs onto the generalized force space. These Jacobians may be obtained by differentiating the joint angles directly. That is, differentiating Eqs. (8) and (10) yield the Jacobian matrices of $\theta_{ha,i}$ and $\theta_{k,i}$, as given in Eqs. (11) and (12), respectively, where $\mathbf{j}_{s,i}$ is the Jacobian of $\mathbf{s}_i$.

$$\mathbf{j}_{ha,i} = \frac{\cos^2\theta_{ha,i}}{s_{iz}^2}[s_{iz}, 0, -s_{ix}]\mathbf{j}_{s,i} \tag{11}$$

$$\mathbf{j}_{k,i} = -\frac{\mathbf{s}_i^T\mathbf{j}_{s,i}}{L_{th}L_{sh}\sin\theta_{k,i}} \tag{12}$$

Direct differentiation of $\theta_{hb,i}$ is more challenging due to the addition of two inverse trigonometric functions. Instead, the $y$ component of Eq. (7) maybe used to derive the Jacobian of $\theta_{hb,i}$, which is expanded as

$$L_{th}\sin\theta_{hb,i} + L_{sh}\sin(\theta_{k,i} + \theta_{hb,i}) = s_{iy} \tag{13}$$

Differentiating Eq. (13) and substituting the known Jacobians yield

$$\mathbf{j}_{hb,i} = \frac{[0, 1, 0]\mathbf{j}_{s,i} - L_{sh}\cos(\theta_{k,i} + \theta_{hb,i})\mathbf{j}_{k,i}}{L_{th}\cos\theta_{hb,i} + L_{sh}\cos(\theta_{k,i} + \theta_{hb,i})} \tag{14}$$

As for $\mathbf{j}_{s,i}$, differentiating ${}^S\mathbf{s}_i$ yields

$${}^S\mathbf{R}_P\dot{\mathbf{s}}_i = -\mathbf{v} + (\mathbf{d}_i - \mathbf{p}) \times \boldsymbol{\omega} \tag{15}$$

where $\mathbf{v}$ is the linear velocity of point $P$. Rearranging Eq. (15) and collecting $\mathbf{v}$ and $\boldsymbol{\omega}$ result in the Jacobian of $\mathbf{s}_i$,

$$\mathbf{j}_{s,i} = \begin{bmatrix} -{}^P\mathbf{R}_S & {}^P\mathbf{R}_S(\tilde{\mathbf{d}}_i - \tilde{\mathbf{p}}) \end{bmatrix} \tag{16}$$

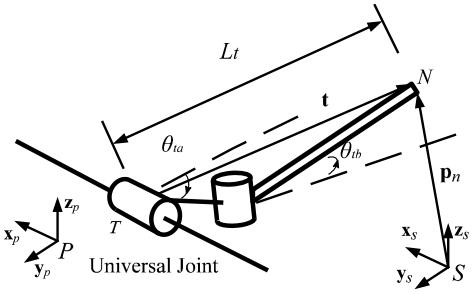


**Fig. 3** Kinematic parameters of the pendulum tail

### *3.1.3 Acceleration relationships and point Jacobian matrices*

Hip and knee point accelerations and Jacobians are required to compute the leg inertia loadings in Sect. 4.1. To find the hip point velocity $\mathbf{v}_{h,i}$ and acceleration $\dot{\mathbf{v}}_{h,i}$, the first and second order differentiation of $H_i$ may be calculated as

$$\mathbf{v}_{h,i} = \mathbf{v} + \boldsymbol{\omega} \times \mathbf{a}_i \tag{17}$$

$$\dot{\mathbf{v}}_{h,i} = \dot{\mathbf{v}} + \tilde{\dot{\boldsymbol{\omega}}}\mathbf{a}_i + \tilde{\boldsymbol{\omega}}^2\mathbf{a}_i \tag{18}$$

For the Jacobians, collecting $\mathbf{v}$ and $\boldsymbol{\omega}$ from Eq. (17) yields

$$\mathbf{J}_{h,i} = \begin{bmatrix} I & -\tilde{\mathbf{a}}_i & \mathbf{0}_{3\times m} \end{bmatrix} \tag{19}$$

Similarly, the velocity, acceleration, and Jacobian matrix of point $K_i$ are obtained by Eq. (20)–(23) where Eq. (23) defines the intermediate matrix $\mathbf{Q}_{k,i}$. We have

$$\mathbf{v}_{k,i} = \mathbf{v} - (\mathbf{a}_i + \mathbf{b}_i) \times \boldsymbol{\omega} + {}^S\mathbf{R}_P\, {}^P\dot{\mathbf{b}}_i \tag{20}$$

$$\dot{\mathbf{v}}_{k,i} = \dot{\mathbf{v}} + \left(\tilde{\dot{\boldsymbol{\omega}}} + \tilde{\boldsymbol{\omega}}^2\right)(\mathbf{a}_i + \mathbf{b}_i) + 2\tilde{\boldsymbol{\omega}}\, {}^S\mathbf{R}_P\, {}^P\dot{\mathbf{b}}_i + {}^S\mathbf{R}_P\, {}^P\ddot{\mathbf{b}}_i \tag{21}$$

$$\mathbf{J}_{k,i} = \left[ \begin{bmatrix} \mathbf{I} & -\tilde{\mathbf{a}}_i - \tilde{\mathbf{b}}_i \end{bmatrix} + {}^S\mathbf{R}_P\mathbf{Q}_{k,i} \begin{bmatrix} \mathbf{j}_{ha,i} \\ \mathbf{j}_{hb,i} \end{bmatrix} \quad \mathbf{0}_{3\times m} \right] \tag{22}$$

$${}^P\dot{\mathbf{b}}_i = L_{th} \begin{bmatrix} -\mathrm{c}\theta_{ha,i}\mathrm{c}\theta_{hb,i} & \mathrm{s}\theta_{ha,i}\mathrm{s}\theta_{hb,i} \\ 0 & \mathrm{c}\theta_{hb,i} \\ \mathrm{s}\theta_{ha,i}\mathrm{c}\theta_{hb,i} & \mathrm{c}\theta_{ha,i}\mathrm{s}\theta_{hb,i} \end{bmatrix} \begin{bmatrix} \dot{\theta}_{ha,i} \\ \dot{\theta}_{hb,i} \end{bmatrix} = \mathbf{Q}_{k,i} \begin{bmatrix} \dot{\theta}_{ha,i} \\ \dot{\theta}_{hb,i} \end{bmatrix} \tag{23}$$

## 3.2 Tail subsystem kinematics

This section models the kinematics of the tail subsystem. Three typical tail structures are considered in this paper – namely, a single-link pendulum tail, a decoupled rolling multi-link rigid tail, and a coupled rolling multi-link flexible tail. These three types represent the most commonly used robotic tail categories in terms of controllability configuration.

### *3.2.1 Pendulum tail kinematics*

As shown in Fig. 3, the pendulum tail consists of only one ideal bar *TN* (an ideal bar is an evenly distributed line mass). The tail connects to the quadruped at point $T$ by a universal joint which is decomposed into two intersecting revolute joints, namely the pitch joint with

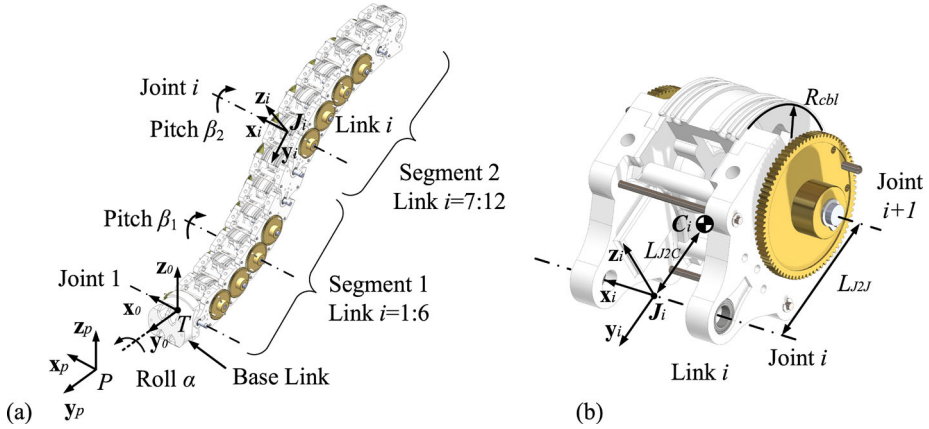


**Fig. 4** (**a**) Kinematic configuration of the R3 tail, (**b**) kinematic definitions for link $i$

rotation angle $\theta_{ta}$ and the yaw joint with rotation angle $\theta_{tb}$. The corresponding generalized coordinate is $\mathbf{q}_t = \begin{bmatrix}\theta_{ta} & \theta_{tb}\end{bmatrix}^T$. Therefore, with parameters defined in Fig. 3, the position of the tail tip $N$ is obtained straightforwardly by Eq. (24) and Eq. (25), where the tail vector $\mathbf{t} = {}^S\mathbf{R}_P\,{}^P\mathbf{t}$, and $\mathbf{R}_x(\theta_{ta})$ and $\mathbf{R}_z(\theta_{tb})$ are the principal rotation matrices with respect to $x$ axis and $z$ axis, respectively. We have

$$\mathbf{p}_n = \mathbf{p} + \mathbf{r} + \mathbf{t} \tag{24}$$

$${}^P\mathbf{t} = \mathbf{R}_x(\theta_{ta})\mathbf{R}_z(\theta_{tb})[0, -L_t, 0]^T \tag{25}$$

The velocity and acceleration of point $N$ are obtained using Eqs. (26)–(28):

$$\mathbf{v}_n = \mathbf{v} - (\mathbf{r} + \mathbf{t}) \times \boldsymbol{\omega} + {}^S\mathbf{R}_P\,{}^P\dot{\mathbf{t}} \tag{26}$$

$$\dot{\mathbf{v}}_n = \dot{\mathbf{v}} + \left(\tilde{\dot{\boldsymbol{\omega}}} + \tilde{\boldsymbol{\omega}}^2\right)(\mathbf{r} + \mathbf{t}) + 2\tilde{\boldsymbol{\omega}}\,{}^S\mathbf{R}_P\,{}^P\dot{\mathbf{t}} + {}^S\mathbf{R}_P\,{}^P\ddot{\mathbf{t}} \tag{27}$$

$${}^P\dot{\mathbf{t}} = L_t \begin{bmatrix} 0 & \mathrm{c}\theta_{tb} \\ \mathrm{s}\theta_{ta}\mathrm{c}\theta_{tb} & \mathrm{c}\theta_{ta}\mathrm{s}\theta_{tb} \\ -\mathrm{c}\theta_{ta}\mathrm{c}\theta_{tb} & \mathrm{s}\theta_{ta}\mathrm{s}\theta_{tb} \end{bmatrix} \begin{bmatrix} \dot{\theta}_{ta} \\ \dot{\theta}_{tb} \end{bmatrix} = \mathbf{K}_n \begin{bmatrix} \dot{\theta}_{ta} \\ \dot{\theta}_{tb} \end{bmatrix} \tag{28}$$

The Jacobian matrix of point $N$ can be obtained accordingly using Eq. (29). Note that the Jacobian and acceleration of point $T$ can be obtained easily by replacing $\mathbf{a}_i$ by $\mathbf{r}$ in Eqs. (18)–(19).

$$\mathbf{J}_n = \begin{bmatrix}\mathbf{I} & -\tilde{\mathbf{r}} - \tilde{\mathbf{t}} & {}^S\mathbf{R}_P\mathbf{K}_n\end{bmatrix} \tag{29}$$

### *3.2.2 R3 tail kinematics*

The kinematic configuration for the R3 tail [29] is shown in Fig. 4, which consists of one base link and twelve serially articulated links. The first six links ($i = 1:6$) constitute one independent segment and the remaining six links ($i = 7:12$) constitute another independent segment. The base link connects to the quadruped torso by a revolute joint (roll $\alpha$) at point $T$. Since the twelve joint axes are all parallel, the tail itself is a planar mechanism. The gears between links are used to evenly distribute the rotations among the joints in each

segment. That is, a rotation of $\beta_j$ ($j = 1$ or 2) degrees in joint $i$ generates a net rotation of $6\beta_j$ degrees for segment $j$. In summary, the R3 tail has three DOFs in total – namely, one overall rolling DOF, one planar bending DOF for the first segment, and one planar bending DOF for the second segment. The corresponding generalized coordinate is chosen as $\mathbf{q}_t = \begin{bmatrix} \alpha & \beta_1 & \beta_2 \end{bmatrix}^T$. The body fixed frames for each link are defined as follows. Frame $\sum T := (T,\ \mathbf{x}_0, \mathbf{y}_0, \mathbf{z}_0)$ is attached on the base link with $\mathbf{x}_0$ coinciding the joint 1 axis and $\mathbf{y}_0$ coinciding $\mathbf{y}_p$. Frame $\sum J_i := (J_i,\ \mathbf{x}_i, \mathbf{y}_i, \mathbf{z}_i)$ is attached on link $i$ with its origin $J_i$ locating on the joint $i$ axis, $\mathbf{x}_i$ coinciding joint $i$ axis, and $\mathbf{y}_i$ pointing along link $i$. Due to the decoupled rolling and bending mobility, the R3 tail is regarded as a representative of decoupled rolling-bending multi-link tail structure. More details on the R3 tail can be found in [29].

With the above kinematic definitions, the orientation for each link is obtained from Eq. (30) where the base link is regarded as link 0.

$$ {}^S\mathbf{R}_i = \begin{cases} {}^S\mathbf{R}_P \mathbf{R}_y(\alpha), & i = 0 \\ {}^S\mathbf{R}_P \mathbf{R}_y(\alpha)\mathbf{R}_x(i\beta_1), & 1 \le i \le 6 \\ {}^S\mathbf{R}_P \mathbf{R}_y(\alpha)\mathbf{R}_x(6\beta_1 + (i-6)\beta_2), & 7 \le i \le 12 \end{cases} \tag{30} $$

The COM position of link $i$ (point $C_i$ in Fig. 4) in inertia frame $\sum S$ may be calculated using Eq. (31) and (32), where $\mathbf{p}_{i,com}$, $\mathbf{p}_{i,jnt}$, and $\mathbf{p}_{i,J2C}$ denotes the position vector of $C_i$, $J_i$, and the vector from $J_i$ to $C_i$, respectively. Note that the base link COM ($C_0$) position $\mathbf{p}_{0,com}$ is given separately as $\mathbf{p}_{0,com} = \mathbf{p} + \mathbf{p}_{0,P2C}$, where $\mathbf{p}_{0,P2C}$ is the vector from point $P$ to $C_0$:

$$ \mathbf{p}_{i,com} = \mathbf{p}_{i,jnt} + \mathbf{p}_{i,J2C} \tag{31} $$

$$ \mathbf{p}_{i,jnt} = \begin{cases} \mathbf{p} + \mathbf{r}, & i = 1 \\ \mathbf{p}_{i-1,jnt} + \mathbf{p}_{i-1,J2J}, & i > 1 \end{cases}; \quad \begin{cases} \mathbf{p}_{i,J2C} = -L_{J2C}\mathbf{y}_i \\ \mathbf{p}_{i,J2J} = -L_{J2J}\mathbf{y}_i \end{cases} \tag{32} $$

The angular velocity propagation formula is obtained by Eq. (33) and the linear velocity is derived by differentiating Eq. (31), as shown in Eq. (34). $\mathbf{v}_{i,jnt}$ and $\mathbf{v}_{i,J2C}$ are calculated by differentiating Eq. (32). The velocity of the base link COM is given as $\mathbf{v}_{0,com} = \mathbf{v} + \boldsymbol{\omega} \times \mathbf{p}_{0,P2C}$. We have

$$ \boldsymbol{\omega}_i = \begin{cases} \boldsymbol{\omega} + \dot{\alpha}\mathbf{y}_0, & i = 0 \\ \boldsymbol{\omega}_{i-1} + \dot{\beta}_1\mathbf{x}_0, & 1 \le i \le 6 \\ \boldsymbol{\omega}_{i-1} + \dot{\beta}_2\mathbf{x}_0, & 7 \le i \le 12 \end{cases} \tag{33} $$

$$ \mathbf{v}_{i,com} = \mathbf{v}_{i,jnt} + \mathbf{v}_{i,J2C} \tag{34} $$

$$ \mathbf{v}_{i,jnt} = \begin{cases} \mathbf{v} + \boldsymbol{\omega} \times \mathbf{r}, & i = 1 \\ \mathbf{v}_{i-1,jnt} + \mathbf{v}_{i-1,J2J}, & i > 1 \end{cases}; \quad \begin{cases} \mathbf{v}_{i,J2C} = \boldsymbol{\omega}_i \times \mathbf{p}_{i,J2C} \\ \mathbf{v}_{i,J2J} = \boldsymbol{\omega}_i \times \mathbf{p}_{i,J2J} \end{cases} \tag{35} $$

Then the Jacobian matrices $\mathbf{J}_{i,\omega}$ and $\mathbf{J}_{i,com}$ for the angular and linear velocities can be obtained recursively by isolating the coefficients in front of the generalized coordinates from Eqs. (33)–(35). $\mathbf{u}_{m,n}$ represents the $m$ dimensional unit column vector with 1 on the $n$th entry, i.e. $\mathbf{u}_{m,n}^T$ is the trivial Jacobian of the $n$th generalized coordinate of $\mathbf{q}$. We have

$$ \mathbf{J}_{i,\omega} = \begin{cases} \begin{bmatrix} \mathbf{0}_{3\times3} & \mathbf{I}_{3\times3} & \mathbf{0}_{3\times3} \end{bmatrix} + \mathbf{y}_0\mathbf{u}_{9,7}^T, & i = 0 \\ \mathbf{J}_{i-1,\omega} + \mathbf{x}_0\mathbf{u}_{9,8}^T, & 1 \le i \le 6 \\ \mathbf{J}_{i-1,\omega} + \mathbf{x}_0\mathbf{u}_{9,9}^T, & 7 \le i \le 12 \end{cases} \tag{36} $$

$$ \mathbf{J}_{i,com} = \mathbf{J}_{i,jnt} + \mathbf{J}_{i,J2C} \tag{37} $$

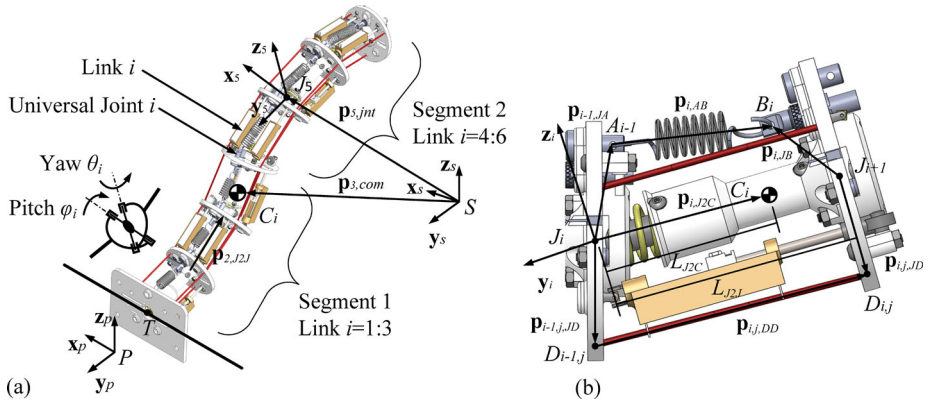


**Fig. 5** (**a**) Kinematic configuration of the USRT tail, (**b**) kinematic definitions for link $i$

$$\mathbf{J}_{i,jnt} = \begin{cases} \begin{bmatrix} \mathbf{I}_{3\times3} & -\tilde{\mathbf{r}} & \mathbf{0}_{3\times3} \end{bmatrix}, & i = 1 \\ \mathbf{J}_{i-1,jnt} + \mathbf{J}_{i-1,J2J}, & i > 1 \end{cases}; \quad \begin{cases} \mathbf{J}_{i,J2C} = -\tilde{\mathbf{p}}_{i,J2C}\mathbf{J}_{i,\omega} \\ \mathbf{J}_{i,J2J} = -\tilde{\mathbf{p}}_{i,J2J}\mathbf{J}_{i,\omega} \end{cases} \tag{38}$$

The linear velocity Jacobian for the base link COM is given separately by Eq. (39):

$$\mathbf{J}_{0,com} = \begin{bmatrix} \mathbf{I}_{3\times3} & -\tilde{\mathbf{p}}_{0,P2C} & \mathbf{0}_{3\times3} \end{bmatrix} \tag{39}$$

The angular and linear acceleration propagation can be obtained by differentiating Eqs. (33)–(35):

$$\dot{\boldsymbol{\omega}}_i = \begin{cases} \dot{\boldsymbol{\omega}} + \ddot{\alpha}\mathbf{y}_0 + \dot{\alpha}\boldsymbol{\omega}_0 \times \mathbf{y}_0, & i = 0 \\ \dot{\boldsymbol{\omega}}_{i-1} + \ddot{\beta}_1\mathbf{x}_0 + \dot{\beta}_1\boldsymbol{\omega}_0 \times \mathbf{x}_0, & 1 \le i \le 6 \\ \dot{\boldsymbol{\omega}}_{i-1} + \ddot{\beta}_1\mathbf{x}_0 + \dot{\beta}_1\boldsymbol{\omega}_0 \times \mathbf{x}_0, & 7 \le i \le 12 \end{cases} \tag{40}$$

$$\dot{\mathbf{v}}_{i,com} = \dot{\mathbf{v}}_{i,jnt} + \dot{\mathbf{v}}_{i,J2C} \tag{41}$$

$$\dot{\mathbf{v}}_{i,jnt} = \begin{cases} \dot{\mathbf{v}} + \tilde{\dot{\boldsymbol{\omega}}}\mathbf{r} + \tilde{\boldsymbol{\omega}}^2\mathbf{r}, & i = 1 \\ \dot{\mathbf{v}}_{i-1,jnt} + \dot{\mathbf{v}}_{i-1,J2J}, & i > 1 \end{cases}; \quad \begin{cases} \dot{\mathbf{v}}_{i,J2C} = \tilde{\dot{\boldsymbol{\omega}}}_i\mathbf{p}_{i,J2C} + \tilde{\boldsymbol{\omega}}_i^2\mathbf{p}_{i,J2C} \\ \dot{\mathbf{v}}_{i,J2J} = \tilde{\dot{\boldsymbol{\omega}}}_i\mathbf{p}_{i,J2J} + \tilde{\boldsymbol{\omega}}_i^2\mathbf{p}_{i,J2J} \end{cases} \tag{42}$$

The acceleration of the base link COM is given by Eq. (43):

$$\dot{\mathbf{v}}_{0,com} = \dot{\mathbf{v}} + \tilde{\dot{\boldsymbol{\omega}}}\mathbf{p}_{0,P2C} + \tilde{\boldsymbol{\omega}}^2\mathbf{p}_{0,P2C} \tag{43}$$

### *3.2.3 USRT kinematic modeling*

The Universal Spatial Robotic Tail (USRT) [26] is another typical multi-link tail structure whose adjacent links are connected by universal joints. This way, the rolling DOF is coupled with the bending DOF, i.e. the rolling motion is achieved by combining the pitch bending and the yaw bending. Due to the elastic elements (elastic backbone and extension springs) used, the USRT is also a representative of flexible tails. The kinematic configuration of the USRT is shown in Fig. 5a where the tail consists of six serially connected universal joints. The first three links constitute the first segment, and the rest three links constitute the second segment. The first segment is driven by two cables $j = \{A, B\}$ from the three cables set $\{1, 2, 3\}$ and the second segment is driven by two cables $j = \{C,\ D\}$ from another three cables set $\{4, 5, 6\}$. For link $i$, the body fixed frame $\sum J_i := (J_i,\ \mathbf{x}_i, \mathbf{y}_i, \mathbf{z}_i)$ is attached at the

center of joint $i$ ($J_i$) with $\mathbf{y}_i$ along with link $i$ axis, and $\mathbf{x}_i$, $\mathbf{z}_i$ coinciding the two rotation axes of the universal joint $i$. $\mathbf{p}_{i,jnt}$ is the position vector of $J_i$, and $\mathbf{p}_{i,com}$ is the position vector of link $i$ COM ($C_i$). More details about the USRT can be found in [26].

Based on the above definitions, link $i$ orientation with respect to both link $i-1$ ($^{i-1}\mathbf{R}_i$) and the global frame ($^{S}\mathbf{R}_i$) are calculated in Eq. (44), where $\varphi_i$ and $\theta_i$ are the decomposed pitch and yaw rotation of the universal joint $i$ (referring to Fig. 5a).

$$^{i-1}\mathbf{R}_i = \mathbf{R}_X(\varphi_i)\mathbf{R}_Z(\theta_i); \quad {}^{S}\mathbf{R}_i = \begin{cases} {}^{S}\mathbf{R}_P, & i=0 \\ {}^{S}\mathbf{R}_{i-1} \cdot {}^{i-1}\mathbf{R}_i, & i>0 \end{cases} \tag{44}$$

The generalized coordinate is chosen as $\mathbf{q}_t = \begin{bmatrix} \theta_1 & \varphi_1 & \cdots & \theta_6 & \varphi_6 \end{bmatrix}^{\boldsymbol{T}}$ accordingly. With these orientations, the joint positions $\mathbf{p}_{i,jnt}$ and the COM positions $\mathbf{p}_{i,com}$ can be calculated recursively using the same formulations as in Eqs. (31)–(32), except replacing the R3RT terms $L_{J2C}$, $L_{J2J}$ with the corresponding USRT ones. The linear velocities, Jacobians, and accelerations of link $i$ could be also calculated using the same formulations as in Eqs. (34)–(35), Eqs. (37)–(38), and Eqs. (41)–(42), respectively. However, the angular propagation formulation is changed due to the different link connections (the USRT uses 2-DOF universal joint while the R3 tail uses 1-DOF revolute joint). Therefore, the angular velocities, Jacobians, and accelerations of the USRT links are calculated according to Eqs. (45)–(47). We have

$$\boldsymbol{\omega}_i = \begin{cases} \boldsymbol{\omega}, & i=0 \\ \boldsymbol{\omega}_{i-1} + \dot{\varphi}_i \mathbf{x}_{i-1} + \dot{\theta}_i \mathbf{z}_i, & i>0 \end{cases} \tag{45}$$

$$\mathbf{J}_{i,\omega} = \begin{cases} \begin{bmatrix} \mathbf{0}_{3\times3} & \mathbf{I}_{3\times3} & \mathbf{0}_{3\times12} \end{bmatrix}, & i=0 \\ \mathbf{J}_{i-1,\omega} + \mathbf{x}_{i-1}\mathbf{u}_{18,2i+6}^T + \mathbf{z}_i\mathbf{u}_{18,2i+5}^T, & i>0 \end{cases} \tag{46}$$

$$\dot{\boldsymbol{\omega}}_i = \begin{cases} \dot{\boldsymbol{\omega}}, & i=0 \\ \dot{\boldsymbol{\omega}}_{i-1} + \ddot{\varphi}_i \mathbf{x}_{i-1} + \dot{\varphi}_i \tilde{\boldsymbol{\omega}}_{i-1}\mathbf{x}_{i-1} + \ddot{\theta}_i \mathbf{z}_i + \dot{\theta}_i \tilde{\boldsymbol{\omega}}_i \mathbf{z}_i, & i>0 \end{cases} \tag{47}$$

Besides the above basic kinematic terms, supplementary kinematic analysis is required to compute the elastic, damping, and the actuation loadings of the USRT. For the compression springs in the center, the net bending angle of each universal joint is obtained by using Eq. (48) where $\mathbf{y}_0 = \mathbf{y}_p$. We have

$$\sigma_i = \cos^{-1}\left(\mathbf{y}_{i-1}^T \mathbf{y}_i\right) \Rightarrow \cos\sigma_i = \cos\theta_i \cos\varphi_i \tag{48}$$

For the extension springs, $\|{}^{i}\mathbf{p}_{i,AB}\|$ is required and obtained by Eq. (49). Similarly, Eq. (50) provides the cable routing vector ${}^{i}\mathbf{p}_{i,DD}$ that is required for the actuation Jacobian calculations:

$${}^{i}\mathbf{p}_{i,AB} = -L_{J2J}\mathbf{e}_y + {}^{i}\mathbf{p}_{i,JB} - {}^{i}\mathbf{p}_{i-1,JA} \tag{49}$$

$${}^{i}\mathbf{p}_{i,j,DD} = -L_{J2J}\mathbf{e}_y + {}^{i}\mathbf{p}_{i,j,JD} - {}^{i}\mathbf{p}_{i-1,j,JD} \tag{50}$$

## 4 Assembly of the dynamics model

Based on the kinematic information obtained (position, velocity, and accelerations), this section calculates the dynamic loading components of Eq. (3) and formulates the forward dynamic model based on the inverse model.

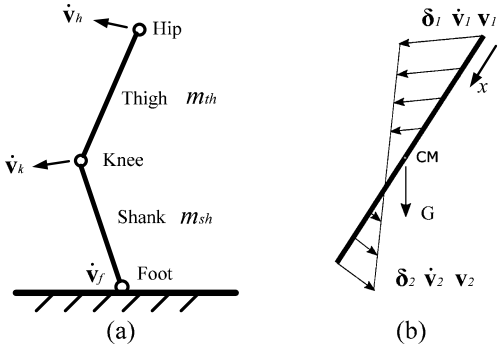


**Fig. 6** (**a**) One leg with its foot touching the ground, (**b**) the velocity distribution on a rigid bar

### 4.1 Quadruped loadings

The quadruped loading calculation includes computing the loading of the torso and the loading of the four legs. For the torso, the loading calculation is straightforward and is given in Eq. (51), in which $m_b$ is the traveling plate mass and g is the gravity constant. The inertia matrix of the traveling plate is calculated as $\mathbf{I}_b = {}^S\mathbf{R}_P\,{}^P\mathbf{I}_b\,{}^P\mathbf{R}_S$. Jacobian matrices $\mathbf{J}_{b,x}$ and $\mathbf{J}_{b,\omega}$ have the form given by Eq. (52):

$$\boldsymbol{\tau}_b = \mathbf{J}_{b,x}^T m_b(\dot{\mathbf{v}} + \mathrm{g}\mathbf{z}_s) + \mathbf{J}_{b,\omega}^T(\mathbf{I}_b\dot{\boldsymbol{\omega}} + \tilde{\boldsymbol{\omega}}\mathbf{I}_b\boldsymbol{\omega}) \tag{51}$$

$$\mathbf{J}_{b,x} = [\,\mathbf{I}_{3\times3} \quad \mathbf{0}_{3\times3} \quad \mathbf{0}_{3\times m}\,]; \qquad \mathbf{J}_{b,\omega} = [\,\mathbf{0}_{3\times3} \quad \mathbf{I}_{3\times3} \quad \mathbf{0}_{3\times m}\,] \tag{52}$$

For the legs, since each thigh and shank is regarded as an ideal bar, the loading may be calculated using the technique in [4]. That is, the virtual work of an ideal bar can be lumped on its two endpoints. As shown in Fig. 6b, for an ideal bar, the virtual work due to the inertia force can be computed by the integral defined in Eq. (53), where the linear interpolations of the virtual displacement $\boldsymbol{\delta}_1$, $\boldsymbol{\delta}_2$, and the acceleration $\dot{\mathbf{v}}_1$, $\dot{\mathbf{v}}_2$ along the bar are defined by Eq. (54). $L$ is the length of the bar. We have

$$\delta W = \int_0^L \boldsymbol{\delta}(x)\cdot\dot{\mathbf{v}}(x)m\,dx/L \tag{53}$$

$$\boldsymbol{\delta}(x) = (1-x/L)\boldsymbol{\delta}_1 + x/L\boldsymbol{\delta}_2; \qquad \dot{\mathbf{v}}(x) = (1-x/L)\dot{\mathbf{v}}_1 + (x/L)\dot{\mathbf{v}}_2 \tag{54}$$

Evaluating Eq. (53) yields Eq. (55), where $\mathbf{q}$ is the generalized coordinate vector, $\mathbf{J}_1$ and $\mathbf{J}_2$ are the corresponding Jacobian matrices for the two endpoints (which implies $\boldsymbol{\delta}_1 = \mathbf{J}_1\delta\mathbf{q}$ and $\boldsymbol{\delta}_2 = \mathbf{J}_2\delta\mathbf{q}$). We have

$$\delta W = \delta\mathbf{q}^T\frac{m}{3}\left(\mathbf{J}_1^T\dot{\mathbf{v}}_1 + \mathbf{J}_2^T\dot{\mathbf{v}}_2 + \frac{\mathbf{J}_2^T\dot{\mathbf{v}}_1 + \mathbf{J}_1^T\dot{\mathbf{v}}_2}{2}\right) \tag{55}$$

Applying this formula on the thigh and shank of each leg (Fig. 6a) yields the virtual work $\delta W_{inr,i}$ of leg $i$ due to inertia force, as given in Eq. (56), where $m_{th}$ and $m_{sh}$ are the mass of the thigh and shank, respectively.

$$\delta W_{inr,i} = \delta\mathbf{q}^T\left[\mathbf{J}_{k,i}^T\left(\frac{m_{th}+m_{sh}}{3}\dot{\mathbf{v}}_{k,i} + \frac{m_{th}}{6}\dot{\mathbf{v}}_{h,i}\right) + \mathbf{J}_{h,i}^T\left(\frac{m_{th}}{3}\dot{\mathbf{v}}_{h,i} + \frac{m_{th}}{6}\dot{\mathbf{v}}_{k,i}\right)\right] \tag{56}$$

The virtual work $\delta W_{grv,i}$ due to gravity is obtained by Eq. (57) and all joints are modeled to be frictionless (including the foot-ground spherical joints). Therefore, the dynamic loading for leg $i$ is obtained by combining Eq. (56) and Eq. (57), as given in Eq. (58):

$$\delta W_{grv,i} = \delta \mathbf{q}^T \left( \mathbf{J}_{k,i}^T \frac{m_{th} + m_{sh}}{2} + \mathbf{J}_{h,i}^T \frac{m_{th}}{2} \right) [0, 0, -\mathrm{g}]^T \tag{57}$$

$$\begin{aligned} \boldsymbol{\tau}_{l,i} = & \mathbf{J}_{k,i}^T \left( \frac{m_{th} + m_{sh}}{3} \dot{\mathbf{v}}_{k,i} + \frac{m_{th}}{6} \dot{\mathbf{v}}_{h,i} + \frac{m_{th} + m_{sh}}{2} \mathrm{g} \mathbf{z}_s \right) \\ & + \mathbf{J}_{h,i}^T \left( \frac{m_{th}}{3} \dot{\mathbf{v}}_{h,i} + \frac{m_{th}}{6} \dot{\mathbf{v}}_{k,i} + \frac{m_{th}}{2} \mathrm{g} \mathbf{z}_s \right) \end{aligned} \tag{58}$$

### 4.2 Tail loadings

For the single-link pendulum tail, the dynamic loading is calculated using the same ideal bar assumption, as shown in Eq. (59), where $\mathbf{J}_t$ and $\dot{\mathbf{v}}_t$ are the Jacobian and acceleration of point $T$, respectively. For the R3 tail, the overall dynamic loading is the sum of the dynamic loadings of each link, as provided in Eq. (60), where $m_{i,r3}$ is the $i$th link mass and $\mathbf{I}_{i,r3} = {}^S\mathbf{R}_i \, {}^i\mathbf{I}_{i,r3} \, {}^i\mathbf{R}_S$ is the $i$th link inertia. Due to its relatively small contribution on the dynamic loading (note that the R3RT has bearings on each joint), the frictions of both the pendulum tail and the R3 tail are neglected in the modeling. We have

$$\boldsymbol{\tau}_t = \mathbf{J}_t^T \frac{m_t}{6} (2\dot{\mathbf{v}}_t + \dot{\mathbf{v}}_n + 3\mathrm{g}\mathbf{z}_s) + \mathbf{J}_n^T \frac{m_t}{6} (2\dot{\mathbf{v}}_n + \dot{\mathbf{v}}_t + 3\mathrm{g}\mathbf{z}_s) \tag{59}$$

$$\boldsymbol{\tau}_t = \sum_{i=0}^{12} \mathbf{J}_{i,com}^T m_{i,r3} (\dot{\mathbf{v}}_{i,com} + \mathrm{g}\mathbf{z}_s) + \mathbf{J}_{i,\omega}^T (\mathbf{I}_{i,r3} \dot{\boldsymbol{\omega}}_i + \tilde{\boldsymbol{\omega}}_i \mathbf{I}_{i,r3} \boldsymbol{\omega}_i) \tag{60}$$

Similarly, the dynamic loading for the USRT could be obtained by adding up the loadings for each link, except that the USRT loading needs to include the additional elastic loadings and the damping loading. Therefore, the total loading of the USRT is calculated by Eq. (61), where the subscripts "inr", "grv", "cmp", "ext" and "dmp" represent "inertia", "gravity", "compression", "extension" and "damping", respectively.

$$\boldsymbol{\tau}_t = \sum_{i=1}^{6} (\boldsymbol{\tau}_{i,inr} + \boldsymbol{\tau}_{i,grv} + \boldsymbol{\tau}_{i,cmp} + \boldsymbol{\tau}_{i,ext} + \boldsymbol{\tau}_{i,dmp}) \tag{61}$$

Due to the shared kinematic terms, the inertia loading and gravity loading are combined together and are given in Eq. (62), where $m_{usrt}$ and $\mathbf{I}_{i,usrt} = {}^S\mathbf{R}_i \, {}^i\mathbf{I}_{usrt} \, {}^i\mathbf{R}_S$ are the mass and inertia matrix of the $i$th link, respectively:

$$\boldsymbol{\tau}_{i,inr} + \boldsymbol{\tau}_{i,grv} = \mathbf{J}_{i,com}^T m_{usrt} (\dot{\mathbf{v}}_{i,com} + \mathrm{g}\mathbf{e}_z) + \mathbf{J}_{i,\omega}^T (\mathbf{I}_{i,usrt} \dot{\boldsymbol{\omega}}_i + \tilde{\boldsymbol{\omega}}_i \mathbf{I}_{i,usrt} \boldsymbol{\omega}_i) \tag{62}$$

The damping and compression spring loadings are both determined by the joint net bending $\sigma_i$. Therefore, $\boldsymbol{\tau}_{i,cmp}$ and $\boldsymbol{\tau}_{i,dmp}$ are derived as

$$\delta W_{i,cmp} = k_{i,cmp} \sigma_i \delta \sigma_i \Rightarrow \boldsymbol{\tau}_{i,cmp} = \mathbf{j}_{i,\sigma}^T k_{i,cmp} \sigma_i \tag{63}$$

$$\delta W_{i,dmp} = c_{i,dmp} \dot{\sigma}_i \delta \sigma_i \Rightarrow \boldsymbol{\tau}_{i,dmp} = \mathbf{j}_{i,\sigma}^T c_{i,dmp} \dot{\sigma}_i \tag{64}$$

where $\mathbf{j}_{i,\sigma}$ (defined by $\delta\sigma_i = \mathbf{j}_{i,\sigma}\delta\mathbf{q}$ and obtained by differentiating Eq. (48)) is the Jacobian matrix for $\sigma_i$. $k_{i,cmp}$ and $c_{i,dmp}$ are the bending stiffness and the damping coefficient of joint $i$, respectively. The virtual work of the extension spring loading is

$$\delta W_{i,ext} = k_{i,ext}\left(\left\|{}^{i}\mathbf{p}_{i,AB}\right\| - L_{i,ext}\right){}^{i}\hat{\mathbf{p}}_{i,AB}\cdot\delta{}^{i}\mathbf{p}_{i,AB} \tag{65}$$

where $k_{i,ext}$ and $L_{i,ext}$ are the stiffness and the unloaded length of spring $i$. ${}^{i}\hat{\mathbf{p}}_{i,AB}$ represents the unit vector of ${}^{i}\mathbf{p}_{i,AB}$. The virtual displacement $\delta{}^{i}\mathbf{p}_{i,AB}$ may be obtained using Eq. (66), where $\mathbf{e}_x = [1 \quad 0 \quad 0]^T$ and $\mathbf{e}_z = [0 \quad 0 \quad 1]^T$. We have

$$\delta{}^{i}\mathbf{p}_{i,AB} = -\delta{}^{i}\mathbf{p}_{i-1,JA} = (\delta\varphi_i\mathbf{e}_x + \delta\theta_i\mathbf{e}_z)\times{}^{i}\mathbf{p}_{i-1,JA} \tag{66}$$

Therefore, the extension spring loading is obtained as in Eq. (67), where $\mathbf{u}^T_{18,2i+6}$ is the trivial Jacobian matrix of $\varphi_i$ (defined by $\delta\varphi_i = \mathbf{u}^T_{18,2i+6}\delta\mathbf{q}$):

$$\boldsymbol{\tau}_{i,ext} = \mathbf{u}_{18,2i+6}k_{i,ext}\left(\left\|{}^{i}\mathbf{p}_{i,AB}\right\| - L_{i,ext}\right){}^{i}\hat{\mathbf{p}}^T_{i,AB}\tilde{\mathbf{e}}_x{}^{i}\mathbf{p}_{i-1,JA} \tag{67}$$

### 4.3 Generalized actuation force

Based on Eq. (3), the actual actuation forces are mapped into the generalized force space by multiplying the actuation Jacobians. For the quadruped, the generalized actuation force is obtained:

$$\mathbf{J}^T_{qa}\boldsymbol{\tau}_{qa} = \sum_{i=1}^{4}\left(\mathbf{j}^T_{ha,i,aug}\tau_{ha,i} + \mathbf{j}^T_{hb,i,aug}\tau_{hb,i} + \mathbf{j}^T_{k,i,aug}\tau_{k,i}\right) \tag{68}$$

where $\tau_{ha,i}$, $\tau_{hb,i}$, and $\tau_{k,i}$ are the torques applied on the hip and knee joints of leg $i$, respectively. $\mathbf{j}_{ha,i,aug}$, $\mathbf{j}_{hb,i,aug}$, and $\mathbf{j}_{k,i,aug}$ are the corresponding actuation Jacobian matrices. The subscript "aug" means that these matrices are augmented from the joint Jacobian matrices (given in Eqs. (11), (12) and (14)) by concatenating $\mathbf{0}_{1\times m}$ to their end. Equation (69) defines the actuation Jacobians for each leg joint:

$$\begin{aligned}\mathbf{j}_{ha,i,aug} &= \begin{bmatrix}\mathbf{j}_{ha,i} & \mathbf{0}_{1\times m}\end{bmatrix}\\ \mathbf{j}_{hb,i,aug} &= \begin{bmatrix}\mathbf{j}_{hb,i} & \mathbf{0}_{1\times m}\end{bmatrix}\\ \mathbf{j}_{k,i,aug} &= \begin{bmatrix}\mathbf{j}_{k,i} & \mathbf{0}_{1\times m}\end{bmatrix}\end{aligned} \tag{69}$$

For the tail subsystem, the generalized actuation force of the pendulum tail is straightforward since the actuation torque applies directly on the generalized variable, as shown in Eq. (70):

$$\mathbf{J}^T_{ta}\boldsymbol{\tau}_{ta} = \mathbf{u}_{8,7}\tau_{ta} + \mathbf{u}_{8,8}\tau_{tb} \tag{70}$$

For the R3 tail, the generalized actuation is contributed by three parts, namely the driven torque $\tau_\alpha$ for the rolling joint, the driven cable tension $T_{\beta 1}$ for the first segment and the driven cable tension $T_{\beta 2}$ for the second segment, as given in Eq. (71), where $\mathbf{J}_{\beta 1}$ and $\mathbf{J}_{\beta 2}$ are the corresponding actuation Jacobian matrices.

$$\mathbf{J}^T_{ta}\boldsymbol{\tau}_{ta} = \mathbf{u}_{9,7}\tau_\alpha + \mathbf{J}^T_{\beta 1}T_{\beta 1} + \mathbf{J}^T_{\beta 2}T_{\beta 2} \tag{71}$$

To compute $\mathbf{J}_{\beta 1}$ and $\mathbf{J}_{\beta 2}$, the virtual works of the first segment and the second segment cable tensions are derived as in Eqs. (72) and (73), where $R_{cbl}$ represents the radius of the circular

cable route (referring to Fig. 4b). Note that $\delta W_{\beta 2}$ is not affected by $\beta_1$ due to the decoupling design of the cable routing [29]. We have

$$\delta W_{\beta 1} = T_{\beta 1} 6 R_{cbl} \delta \beta_1 \Rightarrow \mathbf{J}_{\beta 1}^T = 6 R_{cbl} \mathbf{u}_{9,8} \tag{72}$$

$$\delta W_{\beta 2} = T_{\beta 2} 6 R_{cbl} \delta \beta_2 \Rightarrow \mathbf{J}_{\beta 2}^T = 6 R_{cbl} \mathbf{u}_{9,9} \tag{73}$$

Similarly, the generalized actuation force of the USRT is given in Eq. (74), where the first three cable tensions ($j = 1, 2, 3$) act on the first segment and the last three cable tensions ($j = 4, 5, 6$) act on the second segment. $\mu_j$ is the switching function to decide whether the driving cable is active or not. Then

$$\mathbf{J}_{ta}^T \boldsymbol{\tau}_{ta} = \sum_{j=1}^{6} \mu_j \mathbf{J}_{tj}^T T_j \tag{74}$$

Therefore, to obtain the actuation Jacobians, the virtual work of each cable tension is derived as

$$\delta W_{tj} = \begin{cases} \sum_{i=1}^{3} \delta W_{tij}, & j = 1, 2, 3 \\ \sum_{i=1}^{6} \delta W_{tij}, & j = 4, 5, 6 \end{cases} \tag{75}$$

where $\delta W_{tij} = T_j {}^i\hat{\mathbf{p}}_{i,j,DD} \cdot \delta {}^i\mathbf{p}_{i,j,DD}$ is the virtual work of the $j$th cable on the $i$th link. The cable virtual displacement $\delta {}^i\mathbf{p}_{i,j,DD}$ is calculated further as

$$\delta {}^i\mathbf{p}_{i,j,DD} = -\delta {}^i\mathbf{p}_{i-1,j,JD} = (\delta\varphi_i \mathbf{e}_x + \delta\theta_i \mathbf{e}_z) \times {}^i\mathbf{p}_{i-1,j,JD} \tag{76}$$

Therefore, the actuation Jacobians are obtained:

$$\mathbf{J}_{tj}^T = \begin{cases} \sum_{i=1}^{3} \mathbf{J}_{tij}^T, & j = 1, 2, 3 \\ \sum_{i=1}^{6} \mathbf{J}_{tij}^T, & j = 4, 5, 6 \end{cases} \tag{77}$$

where

$$\mathbf{J}_{tij}^T = \mathbf{u}_{18,2i+5}\left({}^i\hat{\mathbf{p}}_{i,j,DD}^T \tilde{\mathbf{e}}_z {}^i\mathbf{p}_{i-1,j,JD}\right) + \mathbf{u}_{18,2i+6}\left({}^i\hat{\mathbf{p}}_{i,j,DD}^T \tilde{\mathbf{e}}_x {}^i\mathbf{p}_{i-1,j,JD}\right) \tag{78}$$

### 4.4 Forward dynamics

Although Eq. (3) fully defines the system dynamics, it is in an implicit form of $\ddot{\mathbf{q}}$, which is not ready for numerical integration yet. To write Eq. (3) into the form with explicit $\ddot{\mathbf{q}}$, i.e. the forward dynamics, the method in [7] (pages 102–103) may be used. That is, if the inverse dynamics is known as a function $\boldsymbol{\tau} = \mathrm{ID}(\mathrm{model}, \mathbf{q}, \dot{\mathbf{q}}, \ddot{\mathbf{q}})$, the forward dynamics may be obtained using Eq. (79) where $\mathbf{M}$ is the system inertia matrix and $\boldsymbol{\tau}$ is the generalized actuator force.

$$\mathbf{M}\ddot{\mathbf{q}} = \boldsymbol{\tau} - \mathrm{ID}(\mathrm{model}, \mathbf{q}, \dot{\mathbf{q}}, \mathbf{0}) \tag{79}$$

The system inertia matrix could be found using the Composite–Rigid–Body algorithm (CRBA) [7], and it may take the form of Eqs. (80)–(83), where $m_{tail}$ and $\mathbf{I}_{i,tail}$ are the inertial properties of the $i$th link for each tail. $n$, in this case, denotes the link number. For instance, for USRT, $m_{tail} = m_{usrt}$, $\mathbf{I}_{i,tail} = \mathbf{I}_{i,usrt}$, and $n = 6$. We have

$$\mathbf{M} = \mathbf{M}_b + \sum_{i=1}^{4} \mathbf{M}_{l,i} + \sum_{i=1}^{n} \mathbf{M}_{i,tail} \tag{80}$$

$$\mathbf{M}_b = m_b \mathbf{J}_{b,x}^T \mathbf{J}_{b,x} + \mathbf{J}_{b,\omega}^T \mathbf{I}_b \mathbf{J}_{b,\omega} \tag{81}$$

$$\mathbf{M}_{l,i} = \frac{m_{th}}{3}\left(\mathbf{J}_{h,i}^T \mathbf{J}_{h,i} + \mathbf{J}_{k,i}^T \mathbf{J}_{k,i} + \mathbf{J}_{h,i}^T \mathbf{J}_{k,i}\right) + \frac{m_{sh}}{3} \mathbf{J}_{k,i}^T \mathbf{J}_{k,i} \tag{82}$$

$$\mathbf{M}_{i,tail} = m_{tail} \mathbf{J}_{i,com}^T \mathbf{J}_{i,com} + \mathbf{J}_{i,\omega}^T \mathbf{I}_{i,tail} \mathbf{J}_{i,\omega} \tag{83}$$

Although the CRBA is efficient and analytical, programming of this algorithm is time consuming and error prone. Instead, an easier way is to take advantage of the existing inverse dynamics function. That is, the $\alpha$th column of $\mathbf{M}$ could be numerically obtained by passing a unit acceleration vector $\boldsymbol{\delta}_\alpha$ to the inverse dynamics function and finding its difference with the zero acceleration case, as shown in Eq. (84). $\boldsymbol{\delta}_\alpha$ has 1 on the $\alpha$th entry and zeros elsewhere. This approach is not as efficient as the CRBA due to its multiple call of the inverse dynamic function, but it is straightforward and usually easy to implement. Therefore, in this paper, we applied the inverse dynamic approach for the pendulum case and the R3RT case due to its easier programming, and applied the CRBA approach for the USRT case due to its higher efficiency. We have

$$\mathbf{m}_\alpha = \mathrm{ID}(\mathrm{model}, \mathbf{q}, \dot{\mathbf{q}}, \boldsymbol{\delta}_\alpha) - \mathrm{ID}(\mathrm{model}, \mathbf{q}, \dot{\mathbf{q}}, \mathbf{0}) \tag{84}$$

## 5 Comparative study of robotic tail structures through numerical experiments

This section uses the established unified dynamics to investigate the dynamic performance of the three typical tail structures. Table 1 summarizes the constants used in the numerical experiments. $D_w$ and $D_l$ are the width and length of the torso rectangle. $k_{i,ext}$ and $L_{i,ext}$ are given in row vector forms. To make the three tails have the same overall properties, the mass, inertia, and spring stiffness of the USRT are scaled accordingly. Note that the index $i$ has different meanings in different contexts. For instance, $i$ represents the leg number in the quadruped modeling but denotes the link number in the multi-link tail modeling. Therefore, the $\mathbf{d}_i$ vectors define the quadruped feet positions, while the ${}^i\mathbf{p}_{i,JA}$, ${}^i\mathbf{p}_{i,JB}$, and ${}^i\mathbf{p}_{i,j,JD}$ vectors belong to the USRT parameters.

The numerical calculations are all implemented in MATLAB, where the built-in solver *ode45* is used to integrate the forward dynamics. This solver uses single step Runge–Kutta (4, 5) method as the numerical integrator and applies variable step scheme to control the error. In this work, the solver accuracy is set to 1e−8 for absolute tolerance and 1e−6 for relative tolerance. The modeling framework in this paper was also cross validated using a commercial software MSC/Adams [14].

Figure 7 shows three configurations of the three quad-tail models. For all simulations, the initial position and orientation of the quadruped are set to be $\mathbf{p} = [0 \quad 0 \quad 0.4]^T$ and $\boldsymbol{\phi} = [0 \quad 0 \quad 0]^T$, respectively. The quadruped input torque is calculated as

$$\boldsymbol{\tau}_{qa} = \begin{bmatrix} 0 & 1.63 & 7.7 & 0 & 1.63 & 7.7 & 0 & 1.9 & 7.16 & 0 & 1.9 & 7.16 \end{bmatrix}^T \mathrm{N\,m} \tag{85}$$

**Table 1** Quadruped-tail model properties

| Var. | Value | Var. | Value |
|---|---|---|---|
| $L_{th}$ | 0.25 m | g | $9.8\ \mathrm{m}\cdot\mathrm{s}^{-2}$ |
| $L_{sh}$ | 0.25 m | ${}^{P}\mathbf{I}_b$ | $\mathrm{diag}(D_l^2, D_w^2, D_l^2 + D_w^2)\ m_b/12$ |
| $D_w$ | 0.3 m | $L_{J2J}$ | R3 : 0.04 m, USRT : 0.08 m |
| $D_l$ | 0.5 m | $L_{J2C}$ | R3 : 0.0327 m, USRT : 0.0466 m |
| $m_b$ | 12 kg | ${}^{0}\mathbf{I}_{0,r3}$ | $\mathrm{diag}(4.33, 3.67, 4.04)10^{-5}\ \mathrm{kg\,m^2}$ |
| $m_{th}$ | 1.2 kg | $m_{\{1-12\},r3}$ | 0.0759 kg |
| $m_{sh}$ | 1.2 kg | ${}^{i}\mathbf{I}_{\{1-12\},r3}$ | $\mathrm{diag}(8.13, 16.26, 18.68)10^{-5}\ \mathrm{kg\,m^2}$ |
| $L_t$ | 0.48 m | ${}^{i}\mathbf{I}_{usrt}$ | $\mathrm{diag}(17.41, 8.3, 16.6)10^{-5}\ \mathrm{kg\,m^2}$ |
| $m_t$ | 1 kg | $k_{i,cmp}$ | $20\ \mathrm{N}\cdot\mathrm{m/rad}$ |
| $R_{cbl}$ | 0.025 m | $c_{i,dmp}$ | $1\ \mathrm{N}\cdot\mathrm{m}\cdot\mathrm{s/rad}$ |
| $m_{0,r3}$ | 0.0897 kg | $k_{ext}$ | (2921.2, 2921.2, 1369.4, 910.6, 245.2, 245.2) N/m |
| $m_{usrt}$ | 0.17 kg | $L_{ext}$ | (38.35, 38.35, 36.83, 36.83, 37.59, 37.59) mm |
| $R_{hl}$ | 0.0325 m | ${}^{i}\mathbf{p}_{i,JA}$ | $[\,0 \quad 0 \quad 0.0305\,]^T$ |
| $\gamma_j$ | $120°\,j - 90°$ | ${}^{i}\mathbf{p}_{i,JB}$ | $[\,0 \quad 0.0225 \quad 0.021\,]^T$ |
| $\epsilon_i$ | $90°\,i - 45°$ | ${}^{i}\mathbf{p}_{i,j,JD}$ | $R_{hl}[\,\cos\gamma_j \quad 0.0035 \quad \sin\gamma_j\,]^T$ |
| | | $\mathbf{d}_i$ | $\sqrt{2}/2[\,D_w\cos\epsilon_i \quad D_l\sin\epsilon_i \quad 0\,]^T$ |

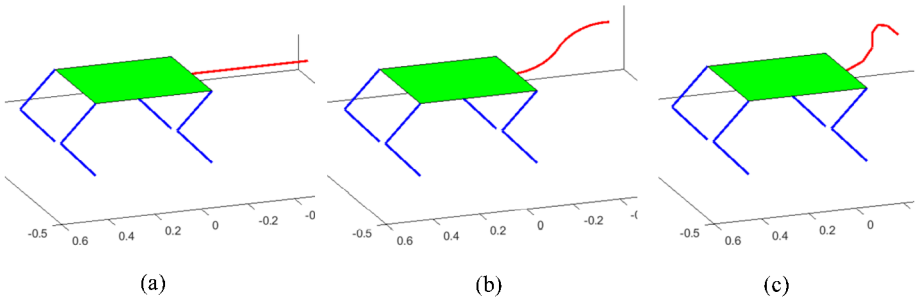


**Fig. 7** Three quadruped models with (**a**) the pendulum tail, (**b**) the R3 tail, and (**c**) the USRT

by the inverse dynamics, to make the quadruped overcome the gravity and maintain relative stability during the simulation. Note that other than the input in Eq. (85), there is no additional torque (such as the feedback torque coming from a feedback controller) applied on the quadruped, which makes the quadruped subsystem essentially an open-loop control system. The reason for this is that, since this paper aims to investigate the dynamic effects of different tail structures, using a controller on the quadruped will make it impossible to determine if the quadruped response is due to the tail motion or the controller. To be consistent with previously reported results in [24] and [14], most simulation durations are chosen to be 0.3 seconds.

The pendulum tail motion is planned as a point-to-point trajectory in the joint space using cubic interpolation, and a simple PD controller is used to track the trajectory (with tracking errors less than 0.5 degrees). To compare the tail performances due to different structures, the tail motions are planned to have the same COM trajectory. This way, the dynamic effect due to different motions could be minimized. Therefore, the R3RT and the

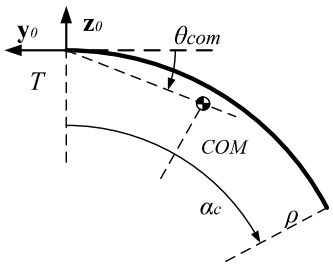


**Fig. 8** Illustration of the COM bending angle of an arc

USRT need to prescribe their curvature bending motion so that their COM would always have the same rotation angle as the pendulum tail case. Referring to Fig. 8, using simple geometry, the formula to compute the COM rotation angle $\theta_{com}$ for a curvature bending arc (non-extensible evenly distributed mass) is given in Eq. (86), where $\alpha_c$ is the central angle. We have

$$\tan(\theta_{com}) = \frac{\alpha_c - \sin\alpha_c}{1 - \cos\alpha_c} \tag{86}$$

### 5.1 Single-link tail structure versus multi-link tail structure

One critical argument for using the multi-link structure for robotic tail is that this structure can generate higher inertia loading than a single-link structure. Existing evidence supporting this argument includes the theoretical analysis in [24] and the experimental exploration in [29]. However, due to the restricted scenarios (only yaw bending) considered in [24] and the tail-only experiments in [29], both research efforts are considered incomplete. Therefore, this section continues the analysis by comparing the pendulum tail (Fig. 7a) and the R3 tail (Fig. 7b) performances on a quadruped, using the more complete quad-tail model established in this paper.

Two sets of experiments were designed to compare the difference: one is a pure bending motion of the tail (mainly used for maneuvering tasks) and one is a pure rolling motion of the tail (mainly used for stabilization tasks). Figure 9 shows the torso responses for two pure bending cases: a 40 degrees yaw bending and an 80 degrees yaw bending. For the R3RT, to execute the yaw bending motion, the roll joint is rotated by $-90$ degrees first so that the tail bending plane could go from the sagittal plane to the transverse plane. In this and the following figures, "PT" stands for the pendulum tail case, "R3" stands for the R3 tail case, and "USRT" stands for the USRT case. From the torso responses, it is found that the torso roll is significantly affected by the yaw bending even though there is no input for the rolling motion. This is because the tail COM moves to the right side and results in more weight on the right side during bending. This effect becomes more significant for larger bending angles, e.g. the roll angle increases for the 80 degrees bending case. However, the torso pitch is not severely affected. The results also indicate that, if the COM rotation angle (instead of the first link rotation angle used in previous research [24]) is used as the benchmark, the one segment (the R3 tail in this experiment is treated as one segment by letting $\beta_1 = \beta_2$) curvature bending of the multi-link structure exhibits similar behavior as the single-link structure. In other words, the curvature bending of the multi-link structure is dynamically similar to a single-link pendulum during bending if COM criterion is used. To justify this statement more rigorously, more yaw bending cases with 10 degrees interval were tested. The results are illustrated in Fig. 10, where the pendulum tail and the R3 tail share similar trends with small differences. From Fig. 10, it is also found that the multi-link structure (R3

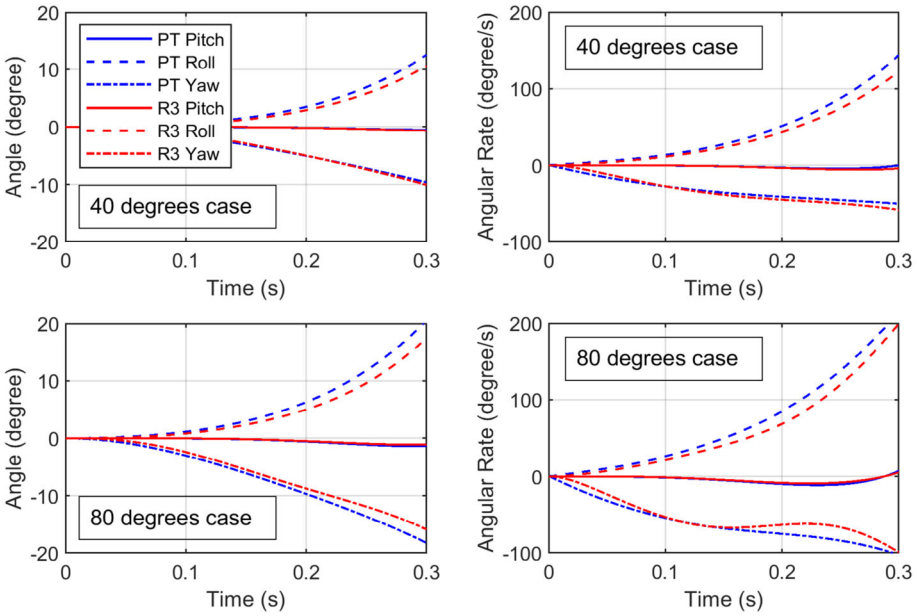


**Fig. 9** Torso responses for a 40 degrees yaw bending case and an 80 degrees yaw bending case where the left column shows the orientation angles while the right column illustrates the corresponding angular rate

**Fig. 10** Torso net yaw rotation with respect to different tail bending angles

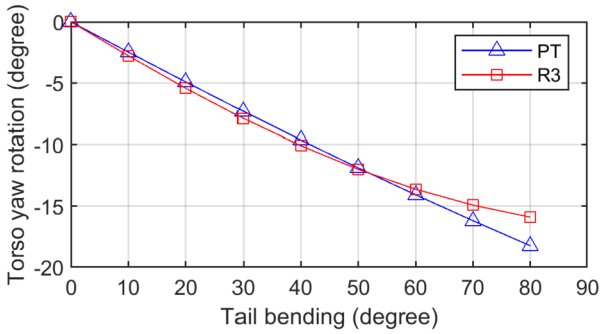


tail) even generates less torso yaw rotation than the single-link structure (pendulum tail) for more than 50 degrees bending cases. This is due to the fact that, for multi-link structures, the last link tends to meet the first link (roll-up) when the bending angle is large, which will make the COM closer to the first link and thus decrease the generated momentum.

The pure rolling experiments are designed as follows. During each simulation, the R3 tail shape remains unchanged ($\dot{\theta}_{com} = 0$) and rotates only the roll joint from 0 degrees to 45 degrees. Among simulations, the R3 tail shape is changed for different COM angle $\theta_{com}$. The pendulum tail is planned to execute the same rolling motion while maintaining the same $\theta_{com}$ as the R3 tail. Note that, since the pendulum tail does not have a separate rolling joint, the rolling motion is achieved by combining the yaw joint rotation and the pitch joint rotation simultaneously. Figure 11 shows the time responses of the torso orientation and their angular rate for two R3 tail shapes ($\theta_{com} = 40°$ and $\theta_{com} = 80°$). Similar to the yaw bending cases,

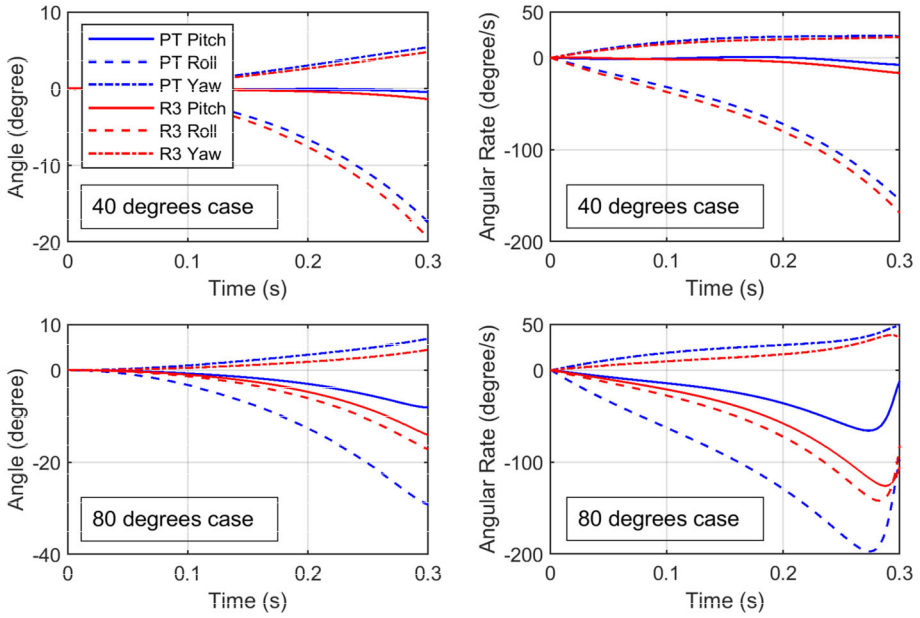


**Fig. 11** Torso responses for the two rolling experiments: the first row maintains $\theta_{com} = 40°$ and the second row maintains $\theta_{com} = 80°$

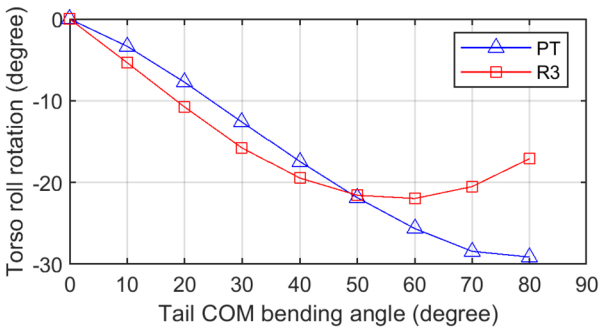


**Fig. 12** Torso net roll rotation with respect to different COM bending angles

the rolling experiments show the same coupling effects between the tail subsystem and the quadruped subsystem. For instance, the torso's yaw and pitch motions are both affected by the tail's rolling motion. More specifically, the yaw motion is affected more significantly but is relatively not sensitive to different tail shapes. The pitch motion, instead, shows strong correlation with tail shapes, i.e. rolling with larger $\theta_{com}$ generates larger pitch rotations. As for the roll responses, the curvature bending structure (R3 tail) was found to generate larger (11.6% more) roll rotation than the single-link structure (pendulum tail) for the 40 degrees tail shape, but generates significantly smaller (41.4% less) roll rotation for the 80 degrees case. This is thought due to the same tail roll up effect as discussed in the yaw bending experiments.

Figure 12 applies the same 10 degrees interval for $\theta_{com}$ to conduct the pure rolling experiments. The results show that the roll-up effect helps the R3 tail generate more momentum

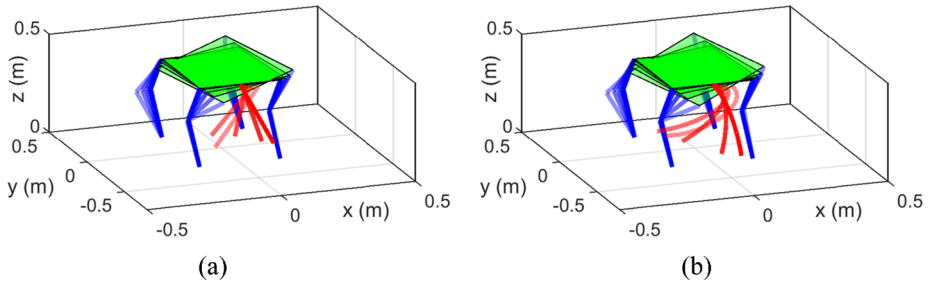


**Fig. 13** Time-lapses of the coupled rolling experiments for (**a**) the Quad-PT model and (**b**) the Quad-R3 model. Each frame has the same time interval of 0.06 s and the transparency increases as time elapses

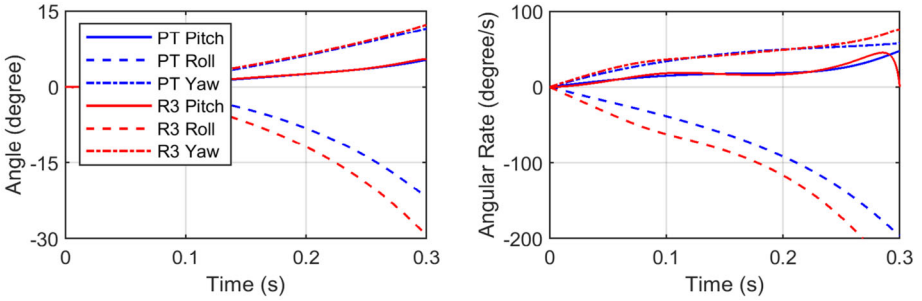


**Fig. 14** Torso responses for the coupled rolling experiments: the left subfigure shows the orientation angles while the right subfigure illustrates the corresponding angular rate

than the pendulum tail before 50 degrees but undermines the benefits significantly after 50 degrees.

### 5.2 Decoupled rolling tail structure versus coupled rolling tail structure

Since the R3 tail has a separate roll joint, it is thought that this tail structure is better on the stabilization tasks. However, a separate roll joint also means that it is not able to generate the motion perpendicular to the bending plane. To do this, the tail has to rotate the bending plane to the desired plane first and then bend. This may cause a delayed response and a more complicated motion planner. In contrast, the universal joint used by the pendulum tail allows the tail to go in any direction and to achieve rolling motion by combining the pitch joint rotation and the yaw joint rotation. Therefore, this subsection investigates the dynamic differences of these two tail mobility configurations.

The tail motion is designed to have a nonlinear combination of yaw motion and pitch motion. That is, the pitch joint of the pendulum tail moves from 20 degrees to 0 degrees and the yaw joint moves from 0 degrees to $-50$ degrees simultaneously. The total effect is that the tail swings up and left. Note that, since the cubic interpolation is nonlinear and the interpolation happens in the joint space, the tail's trajectory in frame $\sum T$ is not a planar motion. The corresponding R3 tail trajectory can be generated using Eq. (86).

The simulation results are shown in Figs. 13 and 14, where Fig. 13 illustrates the time-lapse images of the two case studies and Fig. 14 plots the torso responses. Based on Fig. 14, the pendulum tail and the R3 tail exhibit very close behaviors for the pitch motion and the

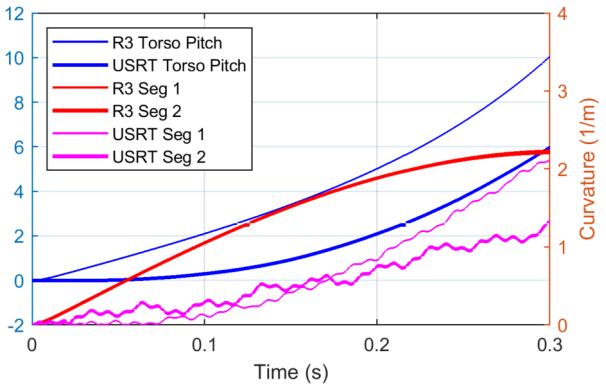


**Fig. 15** Torso and tail curvature responses for the 20 degrees pitch bending experiments

yaw motion, but for the rolling motion, the R3 tail generates 33.2% larger torso roll rotation than the pendulum tail. By comparing this phenomenon with those in Figs. 11 and 12, this larger rolling rotation for the R3 tail is found due to its larger rolling angle (90 degrees). Therefore, from solely a dynamics perspective, the decoupled rolling tail structure does not show a significant difference from the coupled rolling structure.

### 5.3 Rigid tail structure versus flexible tail structure

The USRT is the multi-link version of the pendulum tail except that it uses elastic components (the compression and extension springs) to constrain the hyper-redundant DOFs. This makes the USRT a flexible robotic tail and makes its dynamics an under-actuated system. This section explores the dynamic performance of this tail structure.

The tail is designed to execute a pure pitch bending motion using a sine wave with amplitude of 20 degrees and period of 1.2 seconds. Figure 15 illustrates the responses of the torso pitch and the tail curvature for the R3 tail and the USRT cases. The R3 tail and the USRT qualitatively exhibit similar dynamic effects on the quadruped. However, the R3 tail generates 4 degrees more (66.6%) rotation than the USRT. The USRT also shows noticeable oscillations induced by its flexible structure. Figure 16 depicts the curvature tracking errors for the two case studies. The USRT shows larger and less smooth tracking errors than the R3 tail, which is consistent with the observations in Fig. 15. The mean errors are calculated as $0.07\ \mathrm{m}^{-1}$, $0.07\ \mathrm{m}^{-1}$, $-0.57\ \mathrm{m}^{-1}$, and $-0.69\ \mathrm{m}^{-1}$ for the R3 tail's first segment, R3 tail's second segment, USRT's first segment, and USRT's second segment, respectively. Apparently, it is the rigidity in the R3 tail that reduces the oscillation and brings in the higher tracking accuracy during highly dynamic motions. This suggests that, for future biomimetic tail designs, variable stiffness ability could be introduced to make the tail maintain the compliant-to-object ability for low dynamic tasks but behave rigidly for highly dynamic tasks. In fact, guided by this observation, one recent development of the multi-link robotic tails is based on the rigid link transmission [15]. This special structure enhances the tail rigidity and thus enables it to bear higher dynamic loading.

## 6 Conclusions and future work

To investigate the dynamic effects of multi-link tails on a quadruped, a high fidelity unified dynamic model incorporating both the quadruped subsystem and the tail subsystem was

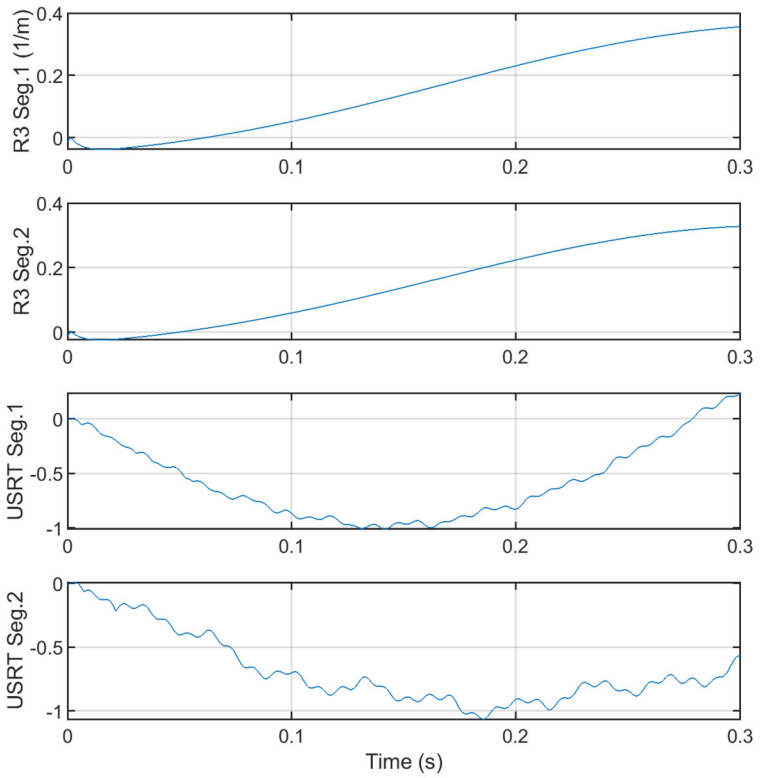


**Fig. 16** Curvature tracking errors for the R3 tail and the USRT case studies

established in this paper. Due to the modularity of the tail subsystem, virtual work-based formulation was applied to generate the overall dynamic framework. Dynamic components of each subsystem were then calculated and assembled into the framework. Based on the new unified dynamic model, three typical tail structures were studied and compared: a single-link pendulum tail, a multi-link rigid tail (the R3 tail), and a multi-link flexible tail (the USRT). Using the COM angle as the benchmark, the comparative study showed that the multi-link structure does not provide significant benefits in comparison with the single-link structure for bending motion but do have noticeable better dynamic performances for rolling motions. The results also showed that the coupled rolling tail structure has no significant differences from the decoupled rolling structure. The USRT case study illustrated obvious oscillations induced by the elastic components in the tail. This disadvantage may limit its usage on highly dynamic applications, but it also suggests that a variable stiffness tail might become a promising solution for the biomimetic robotic tail design.

To eliminate the influence of the discontinuous locomotion dynamics on the tail analysis, the unified dynamic model in this paper fixed the quadruped feet on the ground. Therefore, one important future work is to relieve this constraint and introduce the hybrid dynamics into the model. This improvement will allow the model to explore more complicated tail behaviors observed in nature. Moreover, validation of the dynamic model on a physical platform would be another focus. As stated in the introduction, the new unified dynamic model will be also used as a tail synthesis platform.

## References

1. Briggs, R., Lee, J., Haberland, M., Kim, S.: Tails in biomimetic design: analysis, simulation, and experiment. In: Proceedings of the IEEE/RSJ International Conference on Intelligent Robots and Systems, Vilamoura, Portugal (2012)
2. Casarez, C.S., Fearing, R.S.: Steering of an underactuated legged robot through terrain contact with an active tail. In: Proceedings of the IEEE/RSJ International Conference on Intelligent Robots and Systems, Madrid, Spain (2018)
3. Chang-Siu, E., Libby, T., Tomizuka, M., Full, R.J.: A lizard-inspired active tail enables rapid maneuvers and dynamic stabilization in a terrestrial robot. In: Proceedings of the IEEE/RSJ International Conference on Intelligent Robots and Systems, San Francisco, USA (2011)
4. Codourey, A.: Dynamic modeling of parallel robots for computed-torque control implementation. Int. J. Robot. Res. **17**(12), 1325–1336 (1998)
5. Dawson, R.S., Warburton, N.M., Richards, H.L., Milne, N.: Walking on five legs: investigating tail use during slow gait in kangaroos and wallabies. Aust. J. Zool. **63**(3), 192–200 (2015)
6. De, A., Koditschek, D.E.: Parallel composition of templates for tail-energized planar hopping. In: Proceedings of the IEEE International Conference on Robotics and Automation, Seattle, USA (2015)
7. Featherstone, R.: Rigid Body Dynamics Algorithms. Springer, Berlin (2014)
8. Freymiller, G.A., Whitford, M.D., Higham, T.E., Clark, R.W.: Escape dynamics of free-ranging desert kangaroo rats (Rodentia: heteromyidae) evading rattlesnake strikes. Biol. J. Linn. Soc. **127**(1), 164–172 (2019)
9. Heim, S.W., Ajallooeian, M., Eckert, P., Vespignani, M., Ijspeert, A.J.: On designing an active tail for legged robots: simplifying control via decoupling of control objectives. Ind. Robot **43**(3), 338–346 (2016)
10. Hickman, G.C.: The mammalian tail: a review of functions. Mamm. Rev. **9**(4), 143–157 (1979)
11. Jusufi, A., Kawano, D.T., Libby, T., Full, R.J.: Righting and turning in mid-air using appendage inertia: reptile tails, analytical models and bio-inspired robots. Bioinspir. Biomim. **5**(4), 045001 (2010)
12. Libby, T., Moore, T.Y., Chang-Siu, E., Li, D., Cohen, D.J., Jusufi, A., Full, R.J.: Tail-assisted pitch control in lizards, robots and dinosaurs. Nature **481**(7380), 181–184 (2012)
13. Libby, T., Johnson, A.M., Chang-Siu, E., Full, R.J., Koditschek, D.E.: Comparative design, scaling, and control of appendages for inertial reorientation. IEEE Trans. Robot. **32**(6), 1380–1398 (2016)
14. Liu, Y., Ben-Tzvi, P.: Dynamic modeling of a quadruped with a robotic tail using virtual work principle. In: Proceedings of the ASME 2018 International Design Engineering Technical Conferences and Computers and Information in Engineering Conference, Quebec City, Canada (2018)
15. Liu, Y., Ben-Tzvi, P.: Design, analysis, and integration of a new two-degree-of-freedom articulated multilink robotic tail mechanism. J. Mech. Robot. **12**(2), 021101 (2020)
16. Liu, G.H., Lin, H.Y., Lin, H.Y., Chen, S.T., Lin, P.C.: A bio-inspired hopping kangaroo robot with an active tail. J. Bionics Eng. **11**(4), 541–555 (2014)
17. Liu, Y., Wang, J., Ben-Tzvi, P.: A cable length invariant robotic tail using a circular shape universal joint mechanism. J. Mech. Robot. **11**(5), 051005 (2019)
18. Machairas, K., Papadopoulos, E.: On quadruped attitude dynamics and control using reaction wheels and tails. In: Proceedings of the European Control Conference, Linz, Austria (2015)
19. Mistry, M., Buchli, J., Schaal, S.: Inverse dynamics control of floating base systems using orthogonal decomposition. In: Proceedings of the IEEE International Conference on Robotics and Automation, Anchorage AK, USA (2010)
20. Nabeshima, J., Saraiji, M.Y., Minamizawa, K.: Arque: artificial biomimicry-inspired tail for extending innate body functions. In: ACM SIGGRAPH 2019 Posters, Los Angeles, CA, USA (2019)
21. O'Connor, S.M., Dawson, T.J., Kram, R., Donelan, J.M.: The kangaroo's tail propels and powers pentapedal locomotion. Biol. Lett. **10**(7), 20140381 (2014)
22. Ouezdou, F.B., Bruneau, O., Guinot, J.C.: Dynamic analysis tool for legged robots. Multibody Syst. Dyn. **2**(4), 369–391 (1998)
23. Patel, A., Boje, E.: On the conical motion of a two-degree-of-freedom tail inspired by the cheetah. IEEE Trans. Robot. **31**(6), 1555–1560 (2015)
24. Rone, W., Ben-Tzvi, P.: Dynamic modeling and simulation of a yaw-angle quadruped maneuvering with a planar robotic tail. J. Dyn. Syst. Meas. Control **138**(8), 084502 (2016)

25. Rone, W.S., Liu, Y., Ben-Tzvi, P.: Maneuvering and stabilization control of a bipedal robot with a universal-spatial robotic tail. Bioinspir. Biomim. **14**(1), 016014 (2018)
26. Rone, W.S., Saab, W., Ben-Tzvi, P.: Design, modeling, and integration of a flexible universal spatial robotic tail. J. Mech. Robot. **10**(4), 041001 (2018)
27. Saab, W., Rone, W.S., Ben-Tzvi, P.: Robotic tails: a state-of-the-art review. Robotica **36**(9), 1263–1277 (2018)
28. Saab, W., Rone, W.S., Ben-Tzvi, P.: Discrete modular serpentine robotic tail: design, analysis and experimentation. Robotica **36**(7), 994–1018 (2018)
29. Saab, W., Rone, W., Kumar, A., Ben-Tzvi, P.: Design and integration of a novel spatial articulated robotic tail. IEEE/ASME Trans. Mechatron. **24**(2), 434–446 (2019)
30. Santiago, J.L.C., Godage, I.S., Gonthina, P., Walker, I.D.: Soft robots and kangaroo tails: modulating compliance in continuum structures through mechanical layer jamming. Soft Robot. **3**(2), 54–63 (2016)
31. Shah, S.V., Saha, S.K., Dutt, J.K.: Modular framework for dynamic modeling and analyses of legged robots. Mech. Mach. Theory **49**, 234–255 (2012)
32. Simon, B., Sato, R., Choley, J.Y., Ming, A.: Development of a bio-inspired flexible tail systemxs. In: Proceedings of the 12th France-Japan and 10th Europe-Asia Congress on Mechatronics, Tsu, Japan (2018)
33. Tsai, L.W.: Solving the inverse dynamics of a Stewart-Gough manipulator by the principle of virtual work. J. Mech. Des. **122**(1), 3–9 (2000)
34. Wang, J., Gosselin, C.M.: A new approach for the dynamic analysis of parallel manipulators. Multibody Syst. Dyn. **2**(3), 317–334 (1998)
35. Young, J.W., Russo, G.A., Fellmann, C.D., Thatikunta, M.A., Chadwell, B.A.: Tail function during arboreal quadrupedalism in squirrel monkeys (Saimiri boliviensis) and tamarins (Saguinus oedipus). J. Exp. Zool. Part A: Ecol. Genet. Physiol. **323**(8), 556–566 (2015)
36. Zeglin, G.J.: Uniroo – a one legged dynamic hopping robot. Bachelor thesis, Massachusetts Institute of Technology, Cambridge, MA, USA (1991)
37. Zhao, J., Zhao, T., Xi, N., Mutka, M.W., Xiao, L.: Msu tailbot: controlling aerial maneuver of a miniature-tailed jumping robot. IEEE/ASME Trans. Mechatron. **20**(6), 2903–2914 (2015)